Level mixing and anisotropy effect in resonant Raman electron paramagnetic transitions in ruby for *B* perpendicular to *c*

X. Lu,[1] S. Venugopalan,[2] Hyunjung Kim,[3] M. Grimsditch,[4] S. Rodriguez,[1] and A.K. Ramdas[1]
[1]*Department of Physics, Purdue University, West Lafayette, Indiana 47907, USA*
[2]*Department of Physics, State University of New York (SUNY) at Binghamton, Binghamton, New York 13902, USA*
[3]*Department of Physics, Sogang University, Seoul, 121-742, Korea*
[4]*Argonne National Laboratory, Argonne, Illinois 60439, USA*
(Received 26 October 2010; revised manuscript received 20 February 2011; published 17 May 2011)

Doubly resonant Raman electron paramagnetic transitions in ruby (Al_2O_3:Cr^{3+}) have been investigated using dye laser excitation tuned across the range of the Zeeman components of its well-known R_1 emission line. With magnetic field **B** normal to **c**, the optic axis of ruby, it is seen that the Raman electron paramagnetic resonance (EPR) lines exhibit significant intensity enhancements due to the simultaneous occurrence of "in resonance" and "out resonance," as visualized in the Kramers-Heisenberg formalism of inelastic light scattering. The specific Raman EPR features observed in the present study, together with their resonances, however, differ markedly from those observed in our previous investigation with **B** ∥ **c**. These differences can be traced to level mixing effects within the Zeeman multiplet of the $^4A_2$ (ground) state on the one hand, and the negligible value of $g_\perp$ for the $\bar{E}$ (excited) state of the R_1 emission line on the other. Furthermore, we note that with **B**⊥**c** and under resonant conditions, the experimentally observed $\Delta m = \pm 1$ pair of Stokes and anti-Stokes Raman lines are not connected by time-reversal symmetry.

DOI: 10.1103/PhysRevB.83.195126 PACS number(s): 78.30.−j, 76.30.Fc, 78.20.Ls, 78.40.Ha

I. INTRODUCTION

The presence of transition-metal ions in dilute concentrations as substitutional impurities in Al_2O_3, MgO, and $MgAl_2O_4$ leads to many fascinating physical properties, thanks to the unique electronic levels associated with them.[1–3] For example, the deep red color of the celebrated gemstone ruby (Al_2O_3:Cr^{3+}), and its atomic-emission-like sharp fluorescence lines known as R_1 and R_2, are a direct result of the site symmetry and energy level structure of the Cr^{3+} ion, when it randomly replaces Al^{3+} in the sapphire (Al_2O_3) lattice.[4,5] The large lifetime of the excited ($\bar{E}$) state of the R_1 line was successfully exploited by Maiman[6] in the invention of the very first laser in 1960. Studies of the absorption and photoluminescence spectra of ruby, and their Zeeman effect, have also yielded a wealth of information concerning the energy levels of Cr^{3+} ion in the presence of an external magnetic field **B**. These include the precise understanding of the evolution of the Zeeman split levels of the ground and excited states of the R_1 line with **B**, their g factors,[7–10] and possible level mixing effects within the Zeeman multiplet of the $^4A_2$ ground state.

We recently reported[11] the Raman electron paramagnetic resonance (Raman EPR) within the Zeeman multiplet of the $^4A_2$ (ground) and $\bar{E}$ (excited) states of the R_1 line in ruby. This paper (hereafter referred to as Paper I) was mainly devoted to our results with **B** ∥ **c**, the optic axis of ruby. In this geometry, the Zeeman split states of the $^4A_2$ ground state remain pure spin states since there are no level mixing effects. This facilitated the assignments and interpretation of the observed Stokes and anti-Stokes Raman EPR transitions, according to the normal selection rules, $\Delta m = \pm 1, \pm 2$. We also demonstrated in Paper I that the Raman EPR lines experience pronounced double resonances when the incident photon energy ($\hbar\omega_L$) alone is tuned across the region of the Zeeman components of the R_1 line, with **B** held constant. These double resonances arise because the Kramers-Heisenberg conditions[12,13] for both "in resonance" and "out resonance" are simultaneously fulfilled for selected Raman EPR lines, whenever the incident laser photon energy ($\hbar\omega_L$) coincides with any of the six Zeeman components (PL_n, n = 2–7) of the R_1 emission line. We explicitly showed in Paper I that the doubly resonant Raman EPR lines obey the selection rules implicit in the Kramers-Heisenberg picture for both the incident photon ($\hbar\omega_L$) and the scattered photon ($\hbar\omega_S$).

In the present study, we explore how the Raman EPR of Cr^{3+} in ruby, in particular, the resonance enhancements, reflect the Zeeman splittings and their magnetic-field dependence for **B**⊥**c**, in contrast to those for **B**∥**c**. In the former geometry, level mixing effects occur within the Zeeman multiplet of the $^4A_2$ ground state, with sublevels no longer being pure spin states. This feature relaxes the Δm selection rules of Raman EPR lines mentioned above for **B**∥**c**. Furthermore, the g factor of the excited ($\bar{E}$) state of R_1 becomes negligible for **B**⊥**c**, with consequences clearly manifested in the Raman EPR spectra as well. The present paper explores these aspects in detail, leading to a comprehensive understanding of the Raman EPR spectra of ruby and their double resonances in both geometries.

II. RESULTS AND DISCUSSION

Experiments were performed in the right-angle scattering geometry, with **B**⊥**c**. All other details of the samples, of the Fabry-Pérot and grating spectrometers, of the superconducting magnet cryostat, and of the lasers used for excitation are described in Paper I. We first consider the Zeeman components of the R_1 photoluminescence, since these are essential for understanding the Raman EPR spectra. The expected Zeeman transitions of R_1 for both orientations of **B** are shown schematically in Figs. 1(a) and 1(b). Here, we have included

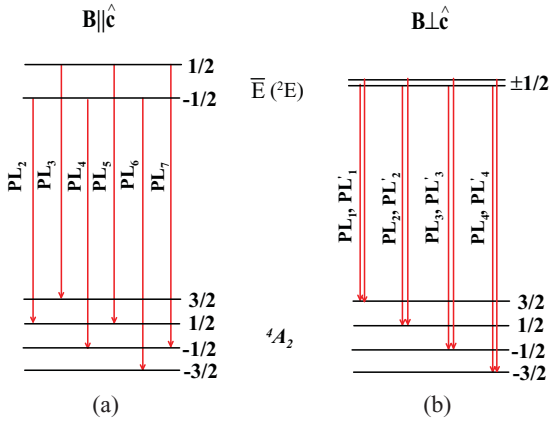

FIG. 1. (Color online) Zeeman components of the R_1 emission line of ruby (a) $\mathbf{B}\|\mathbf{c}$, PL_n ($n = 2$–7), and (b) $\mathbf{B}\perp\mathbf{c}$, ($PL_n$,$PL'_n$) ($n =$ 1–4).

the diagram of the transitions for $\mathbf{B}\|\mathbf{c}$ from Paper I, in order to contrast it with the case of $\mathbf{B}\perp\mathbf{c}$. Note that six distinct Zeeman components occur for $\mathbf{B}\|\mathbf{c}$, labeled PL_n (n = 2–7), in the order of increasing energy. The magnetic-field dependence of these six components is consistent with the following g factors:[9,10] $g_\parallel(^4A_2) = 1.984 \pm 0.0006$, $g_\parallel(\bar{E}) = 2.445 \pm 0.001$. In contrast, for $\mathbf{B}\perp\mathbf{c}$, we expect eight Zeeman components, as shown in Fig. 1(b). This is due to level mixing effects within the Zeeman split levels of the $^4A_2$ ground state, which are hence no longer pure spin states. Thus, the selection rules for dipole transitions ($\Delta m = 0, \pm 1$) are now relaxed, and these transitions can occur between each of the $\bar{E}$ ($\pm 1/2$) excited states and all four sublevels of the $^4A_2$ ground state. Furthermore, we note[9,10] that $g_\perp(\bar{E}) = 0.05$, while $g_\perp(^4A_2) = 1.9867 \pm 0.0006$. The resulting negligible splitting of the $\bar{E}$ ($\pm 1/2$) levels, in turn, must give rise to four distinct components of the photoluminescence of R_1, each of which is itself a closely spaced doublet. In the order of increasing energy, we label each of these doublets as (PL_n,PL'_n), $n = 1$–4. Figure 2(a) shows these eight components clearly resolved at 6 T with a high spectral resolution of $\sim$0.4 cm^{-1}—a resolution which is accessible in PL experiments, given the very large intensity of these PL features. However, at a lower resolution and/or magnetic field, each doublet merges into a single line, which we shall henceforth label as PL^*_n. Thus, for $\mathbf{B}\perp\mathbf{c}$, effectively there are just four PL^*_n lines, $n = 1$–4, in the order of increasing energy. Given the negligible splitting of the $\bar{E}$ excited state, in the following discussion, we will hence assume that the $\bar{E}$ ($\pm 1/2$) states are degenerate. The magnetic-field dependence of the (PL_n,PL'_n) pairs is depicted in Fig. 2(b). The solid lines are calculated using the spin Hamiltonian in Ref. 9 and the known $g_\perp$ values of the ground and excited states of the R_1 line. Figure 3 shows the calculated magnetic-field dependence of the Zeeman levels of the $^4A_2$ ground state. It should be noted that the sublevels labeled here as $-3/2$, $-1/2$, $1/2$, and $3/2$ are no longer pure spin states[9] because of level mixing. At any $\mathbf{B}$, the experimentally observed Raman EPR features, and their shifts, can be independently identified using Fig. 3. Further, it should be noted that whereas Fig. 2(b) depicts the energies of the (PL_n,PL'_n) pairs of luminescence transitions with $\mathbf{B}$, Fig. 3 shows the evolution of the $^4A_2$ ground-state sublevels with $\mathbf{B}$. The latter, together with the negligible value of $g_\perp$ for the $\bar{E}$ ($\pm 1/2$) states, accounts for the slopes seen in Fig. 2(b) for all values of $\mathbf{B}$.

Next, we consider the Stokes and the anti-Stokes Raman EPR spectra associated with the Zeeman multiplet of the $^4A_2$ ground state for $\mathbf{B}\perp\mathbf{c}$. Figure 4(a) shows the spectrum obtained with $\hbar\omega_L = 14\,395$ cm^{-1} and $\mathbf{B} = 6$ T. Given the proximity of this $\hbar\omega_L$ to the Zeeman components of R_1, the intensity of the Raman EPR spectrum in Fig. 4(a) is already enhanced by near-resonant conditions. Indeed, as mentioned in Paper I, lowering $\hbar\omega_L$ by just $\sim$20 cm^{-1} decreases the intensity of the Raman EPR spectrum to such an extent that it becomes

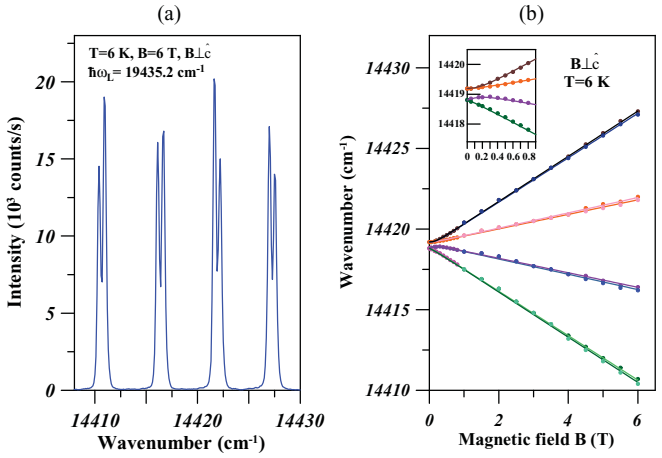

FIG. 2. (Color online) (a) The photoluminescence spectrum of the (PL_n,PL'_n) doublets observed at 6 T. (b) The magnetic-field dependence of (PL_n,PL'_n) doublets. Dots denote experimental data and the solid lines are calculated using the known $g_\perp$ values of the ground and excited states of the R_1 line. Note that there are two nearly overlapping lines corresponding to each (PL_n,PL'_n) doublet, reflecting the very small splitting between the $\bar{E}$ ($\pm 1/2$) excited states of R_1.

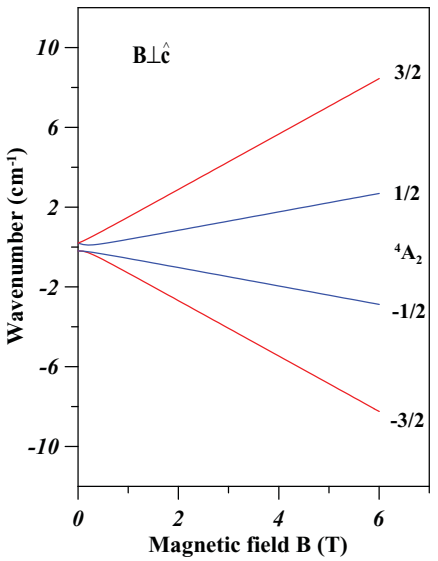

FIG. 3. (Color online) Calculated magnetic-field dependence of the Zeeman sublevels of the $^4A_2$ ground state for $\mathbf{B}\perp\mathbf{c}$.

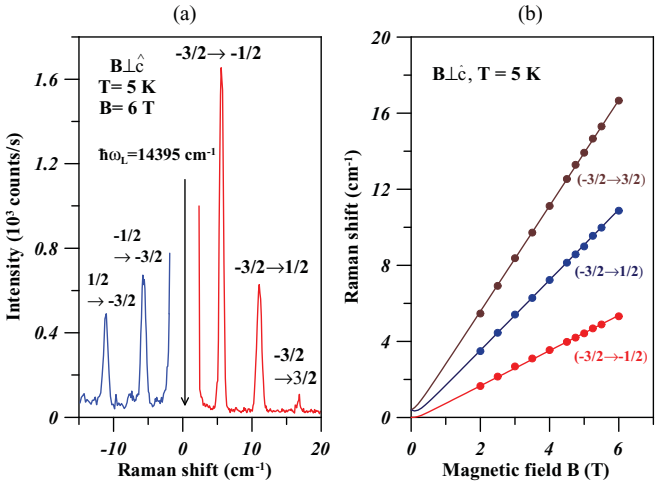

FIG. 4. (Color online) (a) Raman EPR spectrum of Cr^{3+} in ruby for $\mathbf{B}\perp\mathbf{c}$. The Stokes and the anti-Stokes Raman EPR shifts recorded with incident photon energy $\hbar\omega_L = 14395.0\ cm^{-1}$, $\mathbf{B} = 6$ T, and $T = 8$ K. (b) The Raman EPR transition energies as a function of $\mathbf{B}$. The solid lines are calculated results using the spin Hamiltonian for $\mathbf{B}\perp\mathbf{c}$.

unobservable. On the anti-Stokes side, we clearly observe two lines corresponding to $\Delta m = -1$ and -2. These have their counterparts on the Stokes side, with $\Delta m = +1$ and $+2$. In addition, on the Stokes side, we also see a line at $\sim 17\ cm^{-1}$ shift corresponding to $\Delta m = +3$; it is not surprising that the anti-Stokes intensity of this feature is too weak to be seen. The assignments of the observed Stokes and the anti-Stokes lines to specific transitions between the Zeeman levels of the $^4A_2$ state is based on the fact that at $\mathbf{B} = 6$ T and $T = 5$ K, the $^4A_2(-3/2)$ state is the lowest and most populated level. A simple analysis involving the Zeeman split levels of the $\bar{E}$ and the $^4A_2$ states in Fig. 1(b) shows that explicitly including the very small splitting of the $\bar{E}$ $(\pm 1/2)$ states will not, in any case, alter the Raman-EPR features observed in the nonresonant or the resonantly enhanced spectra. A comparison of the spectrum in Fig. 4(a) with the corresponding results in Fig. 3(a) of Paper I, under near-resonant conditions for $\mathbf{B}\|\mathbf{c}$, reveals the following important differences: (1) For $\mathbf{B}\|\mathbf{c}$, a total of five distinct Raman EPR lines occur (one of which is clearly resolved only under exact resonant conditions), whereas for $\mathbf{B}\perp\mathbf{c}$ only three are seen. (2) With $\mathbf{B}\|\mathbf{c}$, three different Raman EPR transitions exist for $\Delta m = \pm 1$, and two for $\Delta m = \pm 2$. In contrast, with $\mathbf{B}\perp\mathbf{c}$, there is just one Raman EPR line corresponding to each of these cases. (3) The feature with $\Delta m = \pm 3$ is absent for $\mathbf{B}\|\mathbf{c}$, since it is forbidden by selection rules. However, level mixing effects relax this selection rule in the present case, since the Zeeman split levels of the $^4A_2$ ground state are no longer pure spin states. The magnetic-field dependence of all three Raman EPR lines is shown in Fig. 4(b). The calculated results based on Fig. 3, shown here as solid lines, agree closely with the experiments.

Results in Paper I clearly demonstrated that when $\hbar\omega_L$ is tuned within the PL_n range, the most relevant intermediate states for the resonantly enhanced Raman EPR spectra of ruby are the $\bar{E}$ $(\pm 1/2)$ excited states of R_1. Strong, doubly resonant enhancement of a pair of Raman EPR lines was observed for $\mathbf{B}\|\mathbf{c}$, whenever the incident photon energy $\hbar\omega_L$ coincides with a PL_n. Then, specific scattered photon energies $(\hbar\omega_S)$ automatically coincide with two different PL_n features, causing both "in" and "out" resonances for the pair of Raman EPR lines involved, in accordance with the Kramers-Heisenberg picture of inelastic light scattering. It was also emphasized in Paper I that the doubly resonant scattering is a two-step process; specifically, there is no matrix element involving an intermediate step, such as electron-phonon interaction[14] or spin-exchange[15] interaction, that separates the transitions corresponding to $\hbar\omega_L$ and $\hbar\omega_S$, and hence these are both energetically related. Furthermore, the selective occurrence of double resonances for both Stokes and anti-Stokes lines, as $\hbar\omega_L$ is tuned within the PL_n range, was pictorially depicted in Fig. 5 of Paper I. In the same spirit, Fig. 5 below illustrates the specific double resonances that will occur for $\mathbf{B}\perp\mathbf{c}$. The energy levels involved for all such double resonances are summarized in Table I. It shows that a coincidence of $\hbar\omega_L$ with a specific PL_n^* results in three distinct scattered photon energies, each one automatically coinciding with one of the other three PL_n^*. Thus, with $\mathbf{B}\perp\mathbf{c}$, both in resonance and out resonance occur simultaneously for three different Raman EPR lines. This contrasts with the results for $\mathbf{B}\|\mathbf{c}$, where two, rather than three, distinct Raman EPR lines undergo simultaneous double resonance whenever $\hbar\omega_L$ coincides with a specific PL_n. As shown in Table I, depending on which PL_n^* fulfills the in-resonance condition, the three different Raman EPR lines which undergo such double resonance can belong to one of the following combinations: (a) anti-Stokes lines only, (b) Stokes lines only, (c) one anti-Stokes and two Stokes lines, or (d) one Stokes and two anti-Stokes lines. Thus, a total of 12 such double resonances of Raman EPR lines will occur as $\hbar\omega_L$ is tuned across the

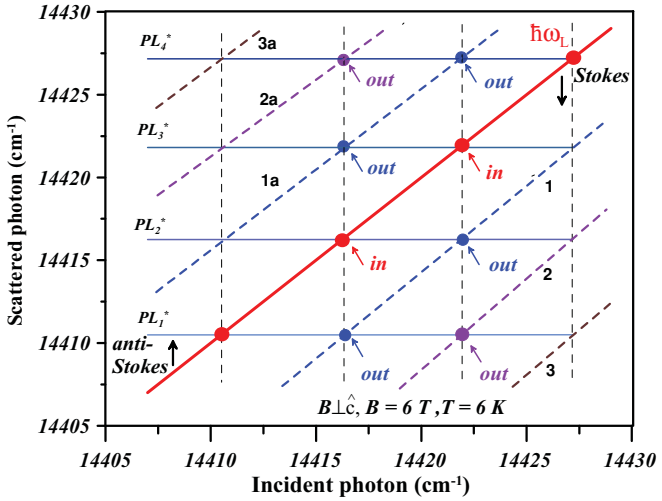

FIG. 5. (Color online) Graphical illustration of the occurrence of double resonances when $\hbar\omega_L$ is scanned across the spectral range of PL_n^* with $\mathbf{B}\perp\mathbf{c}$. Scattered photon energies $\hbar\omega_S$ of Raman EPR lines are parallel to the diagonal line labeled $\hbar\omega_L$. The simultaneous coincidence of $\hbar\omega_L$ and $\hbar\omega_S$ for different PL_n^* is depicted at $\mathbf{B} = 6$ T. The Raman transitions corresponding to each $\hbar\omega_S$ line (1a–3a and 1–3) are given in the text. The photoluminescence lines PL_1^*–PL_4^*, being independent of $\hbar\omega_L$, appear in the figure as horizontal lines parallel to the abscissa.

TABLE I. Selection rules for double resonance of Raman EPR Lines (**B**⊥**c**).

$\hbar\omega_L$	$\hbar\omega_S$	Δm [Raman transition]
$^4A_2(3/2) \rightarrow \bar{E}(\pm 1/2) = PL_1^*$	$\bar{E}(\pm 1/2) \rightarrow {}^4A_2(1/2) = PL_2^*$	$\Delta m = -1[^4A_2(3/2) \rightarrow {}^4A_2(1/2)]$
	$\bar{E}(\pm 1/2) \rightarrow {}^4A_2(-1/2) = PL_3^*$	$\Delta m = -2\left[^4A_2(3/2) \rightarrow {}^4A_2(-1/2)\right]$
	$\bar{E}(\pm 1/2) \rightarrow {}^4A_2(-3/2) = PL_4^*$	$\Delta m = -3\left[^4A_2(3/2) \rightarrow {}^4A_2(-3/2)\right]$
$^4A_2(1/2) \rightarrow \bar{E}(\pm 1/2) = PL_2^*$	$\bar{E}(\pm 1/2) \rightarrow {}^4A_2(3/2) = PL_1^*$	$\Delta m = +1\left[^4A_2(1/2) \rightarrow {}^4A_2(3/2)\right]$
	$\bar{E}(\pm 1/2) \rightarrow {}^4A_2(-1/2) = PL_3^*$	$\Delta m = -1\left[^4A_2(1/2) \rightarrow {}^4A_2(-1/2)\right]$
	$\bar{E}(\pm 1/2) \rightarrow {}^4A_2(-3/2) = PL_4^*$	$\Delta m = -2\left[^4A_2(1/2) \rightarrow {}^4A_2(-3/2)\right]$
$^4A_2(-1/2) \rightarrow \bar{E}(\pm 1/2) = PL_3^*$	$\bar{E}(\pm 1/2) \rightarrow {}^4A_2(3/2) = PL_1^*$	$\Delta m = +2\left[^4A_2(-1/2) \rightarrow {}^4A_2(3/2)\right]$
	$\bar{E}(\pm 1/2) \rightarrow {}^4A_2(1/2) = PL_2^*$	$\Delta m = +1\left[^4A_2(-1/2) \rightarrow {}^4A_2(1/2)\right]$
	$\bar{E}(\pm 1/2) \rightarrow {}^4A_2(-3/2) = PL_4^*$	$\Delta m = -1\left[^4A_2(-1/2) \rightarrow {}^4A_2(-3/2)\right]$
$^4A_2(-3/2) \rightarrow \bar{E}(\pm 1/2) = PL_4^*$	$\bar{E}(\pm 1/2) \rightarrow {}^4A_2(3/2) = PL_1^*$	$\Delta m = +3\left[^4A_2(-3/2) \rightarrow {}^4A_2(3/2)\right]$
	$\bar{E}(\pm 1/2) \rightarrow {}^4A_2(1/2) = PL_2^*$	$\Delta m = +2\left[^4A_2(-3/2) \rightarrow {}^4A_2(1/2)\right]$
	$\bar{E}(\pm 1/2) \rightarrow {}^4A_2(-1/2) = PL_3^*$	$\Delta m = +1\left[^4A_2(-3/2) \rightarrow {}^4A_2(-1/2)\right]$

entire range of PL_n^*. Among these, there are three different Stokes transitions with $\Delta m = +1$, whose Raman shifts are nearly the same within the resolution of our measurements, even at **B** = 6 T. Hence, the $\hbar\omega_S$ line in Fig. 5 (labeled as 1) corresponding to these $\Delta m = +1$ Stokes transitions, viz., $\{^4A_2(-3/2) \rightarrow {}^4A_2(-1/2)$; $^4A_2(-1/2) \rightarrow {}^4A_2(1/2)$; $^4A_2(1/2) \rightarrow {}^4A_2(3/2)\}$, can be considered as a superposition resulting from three closely spaced, and unresolved lines. This also applies to their counterpart, anti-Stokes transitions $\{^4A_2(-1/2) \rightarrow A_2(-3/2)$; $^4A_2(1/2) \rightarrow {}^4A_2(-1/2)$; $^4A_2(3/2) \rightarrow {}^4A_2(1/2)\}$, and the $\hbar\omega_S$ line in Fig. 5 (labeled as 1a) corresponding to $\Delta m = -1$. Considering the $\Delta m = +2$ Stokes transitions in Table I, viz., $\{^4A_2(-3/2) \rightarrow {}^4A_2(1/2)$; $^4A_2(-1/2) \rightarrow {}^4A_2(3/2)\}$, and its corresponding $\hbar\omega_S$ line in Fig. 5 (labeled as 2), we note that they are to be considered as a superposition of two closely spaced, but unresolved, lines. Again, this situation applies to their anti-Stokes counterparts with $\Delta m = -2$, viz., $\{^4A_2(1/2) \rightarrow {}^4A_2(-3/2)$; $^4A_2(3/2) \rightarrow {}^4A_2(-1/2)\}$, and its $\hbar\omega_S$ line in Fig. 5 (labeled as 2a). Finally, we note that the $\Delta m = +3$ transition $\{^4A_2(-3/2) \rightarrow {}^4A_2(3/2)\}$, and the $\Delta m = -3$ transition $\{^4A_2(3/2) \rightarrow {}^4A_2(-3/2)\}$ in Table I and their respective $\hbar\omega_S$ lines, labeled as 3 and 3a in Fig. 5, are free of any such superposition, since there is just one unique Raman transition possible for each of these cases.

Following the approach described in Paper I, in Fig. 5 here the ordinate corresponds to $\hbar\omega_S$ and the abscissa to $\hbar\omega_L$. Since the energies of the photoluminescence lines are independent of $\hbar\omega_L$ utilized in the Raman experiment, the positions of PL_1^*–PL_4^* appear in the figure as four horizontal lines parallel to the abscissa. Also, the diagonal line labeled $\hbar\omega_L$ in this plot, corresponding to incident photon energy, serves as a reference line (i.e., zero-frequency shift line) for locating $\hbar\omega_S$, the Stokes and the anti-Stokes shifts for a given $\hbar\omega_L$; the $\hbar\omega_S$'s lie on lines parallel to $\hbar\omega_L$. The energies of the Raman lines with $\Delta m = \pm 1, \pm 2$, and ± 3, as a function of the tunable dye laser photon energy ($\hbar\omega_L$), are also depicted on this plot; thus one can discover unambiguously the $\hbar\omega_L$'s at which the resonant enhancements of the Raman EPR transitions occur. The four intersections of the horizontal PL lines with the line labeled $\hbar\omega_L$, denoted by full red circles, identify the four incident photon energies for which the conditions for in resonance are fulfilled. Simultaneously, in each such case, there are three distinct Raman EPR lines which fulfill $\hbar\omega_S = PL_n^*$, i.e., out resonance. These out resonances are signaled by the intersections of the $\hbar\omega_S$ lines with the PL lines (located on the vertical dashed lines passing through the corresponding full circle).

Two illustrative examples of the expected double resonances of Raman EPR lines for **B**⊥**c** are shown in Figs. 6(a) and 6(b). In the former, with $\hbar\omega_L = PL_2^*$, three distinct Raman EPR lines are observed with strong resonant enhancement—two anti-Stokes and one Stokes. The corresponding scattered photon transitions are PL_4^*, PL_3^*, and PL_1^*, as shown in the accompanying level diagram. Here, the two $\hbar\omega_S$ transitions causing the anti-stokes Raman EPR lines are indicated as down arrows in blue, whereas that leading to the Stokes Raman EPR line is indicated in dark brown. Note that each Raman EPR transition is indicated by a green arrow. This is indeed confirmed in Fig. 6(a), where we clearly observe two anti-Stokes Raman transitions corresponding to $\Delta m = -1$ and -2, as well as one Stokes Raman transition corresponding to $\Delta m = +1$. The Stokes counterpart of the $\Delta m = -2$ anti-Stokes line is invisible, on the intensity scale here, since it cannot experience double resonance. A reversal of the spectral features seen in Fig 6(a) is evident in Fig. 6(b), where $\hbar\omega_L = PL_3^*$. We now expect to see two doubly resonant Stokes Raman EPR lines, and one doubly resonant anti-Stokes Raman EPR line; the allowed $\hbar\omega_S$ correspond to PL_1^*, PL_2^*, and PL_4^*. These, in turn, cause the doubly resonant Raman EPR transitions corresponding, respectively, to the $\Delta m = +1$ and $+2$ Stokes features and the $\Delta m = -1$ anti-Stokes feature. Again, the spectrum of Fig. 6(b) clearly confirms these predictions.

It is also worth noting that in each spectrum discussed above, the $\Delta m = \pm 1$ lines are not related by time-reversal

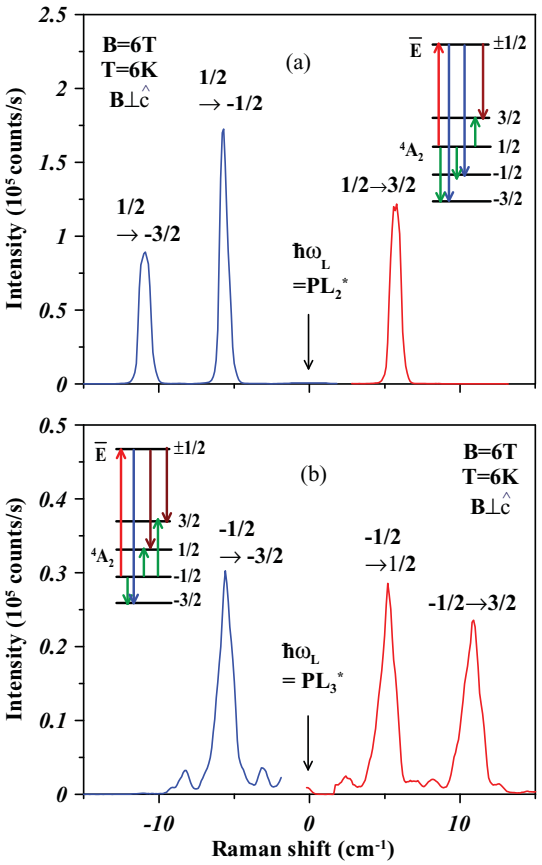

FIG. 6. (Color online) Doubly resonant Raman EPR spectra of ruby for $\mathbf{B}\perp\mathbf{c}$, $\mathbf{B} = 6$ T, and $T = 8$ K. In the insets, scattered photon transitions causing anti-Stokes lines are shown as blue vertical lines, while those causing Stokes transitions are the dark brown vertical lines. The net Raman EPR transition in each case is indicated by the green arrows. In (a) $\hbar\omega_L = \mathrm{PL}_2^*$, and in (b) $\hbar\omega_L = \mathrm{PL}_3^*$.

symmetry, although their frequency shifts are nearly identical. A pair of Stokes and anti-Stokes Raman lines are connected through time-reversal symmetry, only if interchanging the initial and final states of one line leads to the other. In the present case, these lines originate from the same initial state, and terminate on different final states. Notably, the results and analysis in Paper I show that for $\mathbf{B}\|\mathbf{c}$, the pair of resonantly enhanced Raman-EPR lines with $\Delta m = +1$ and $\Delta m = -1$ which can simultaneously undergo double resonance, possess measurably different Raman shifts; hence they cannot be misconstrued as a Stokes:anti-Stokes pair. When $\hbar\omega_L$ lies well outside the range of exact resonant conditions, in both $\mathbf{B}\|\mathbf{c}$ and $\mathbf{B}\perp\mathbf{c}$ geometries, as in Fig. 4(a), the ability to precisely select and identify the initial and final states is absent, and hence we can expect that time reversal symmetry would apply to the Stokes and anti-Stokes pair of lines seen in the nonresonant spectrum.

III. CONCLUDING REMARKS

The present study has elucidated the Raman-EPR transitions of Cr^{3+} in ruby for $\mathbf{B}\perp\mathbf{c}$, under both resonant and nonresonant conditions. The observed Raman EPR lines, and the specific characteristics of their double resonances, differ markedly from the results reported in our previous study of ruby with $\mathbf{B}\|\mathbf{c}$. These differences can be clearly understood on the basis of level mixing effects which occur for $\mathbf{B}\perp\mathbf{c}$ within the ground state ($^4A_2$) Zeeman multiplet of Cr^{3+} in ruby, and the very small value of $g_\perp$ for the $\bar{E}$ intermediate states which participate in the Raman scattering process.

Raman scattering from electronic levels has a rich history,[16] which precedes the use of lasers for the study of Raman spectra. Since tunable lasers became available, it has also been possible to explore their resonant effects and excitation profiles in detail, leading to studies of "in" and "out" resonances in condensed-matter systems; typical examples include the $ErPO_4$ study by Williams *et al.*[17] and the diluted magnetic semiconductors study by Peterson *et al.*[15] In most such cases, in resonance and out resonance are decoupled from each other; i.e., in resonance does not automatically guarantee out resonance. Ruby offers a unique and remarkably different system in this regard; viz., due to the absence of spin-exchange or electron-phonon interaction while the electron is in the intermediate state, in resonance automatically causes out resonance for specific Raman EPR features, at *any* magnetic field. This clearly differs from other typical instances of double resonances of Raman features observed in the solid state[18,19] wherein, in addition to the tuning of $\hbar\omega_L$ in order to realize in resonance, simultaneous and specific tuning of another experimental parameter (e.g., temperature, pressure, magnetic field, etc.) is needed in order to make the scattered photon energy ($\hbar\omega_S$) coincide with a different electronic transition of the medium.

Studies of EPR transitions of Cr^{3+} in ruby were reported by some authors[20–22] in recent years, by employing the technique of direct microwave absorption coupled with Raman heterodyne detection. Specifically, the optically detected EPR transitions they observe in ruby (a) occur only at specific values of $\mathbf{B}$, since the microwave field is of a fixed frequency, and (b) do not replicate the highly resolved Stokes and anti-Stokes Raman EPR signatures we clearly observe for different possible Δm values, including ± 3. Furthermore, direct Raman spectroscopy has allowed us to discover their distinct double resonances at *any* $\mathbf{B}$ field, and exploit them in order to unambiguously assign all of the observed features. Hence we note that in various crucial aspects, including the underlying technique, process, selection rules, and observed spectral features corresponding to different possible Δm values, our Raman experiments have generated results which are distinctly different from their work.

In summary, ruby offers a unique solid-state system wherein clearly resolved, double resonances of both Stokes and anti-Stokes Raman EPR spectral features are realized solely by tuning $\hbar\omega_L$. The electronic Zeeman levels of Cr^{3+} in ruby, through its R_1 transitions, have generated a *unique opportunity* in the context of Raman spectroscopy at its microscopic level. As formulated in the Kramers-Heisenberg theory of Raman transitions, these levels admirably fulfill the roles of "initial, intermediate, and final" states. These exceptionally sharp levels of R_1 presented a unique opportunity to discover all the Raman EPR transitions, and their doubly resonant characteristics. These results for $\mathbf{B}\|\mathbf{c}$ and $\mathbf{B}\perp\mathbf{c}$, while being equally impressive, clearly differ significantly in the underlying physics, as demonstrated in this paper.

ACKNOWLEDGMENTS

X.L., S.R. and A.K.R acknowledge support from the US National Science Foundation (DMR-0405082 and DMR-0705793), M.G. from the US Department of Energy, BES Material Sciences (Grant No. W-31-109-ENG-38), and H.K. from Sogang University Special Research Grant (2009).

[1] *Spectroscopy of Solid-State Laser-Type Materials*, edited by B. Di Bartolo (Plenum, New York, 1987).

[2] D.S. McClure, in *Solid State Physics*, edited by F. Seitz and D. Turnbull (Academic, New York, 1959), Vol. 9, p. 399.

[3] D. L. Wood, G. F. Imbusch, R. M. Macfarlane, P. Kisliuk, and D. M. Larkin, J. Chem. Phys. **48**, 5255 (1968).

[4] A. L. Schawlow, J. Appl. Phys. **33**, 395 (1962).

[5] F. Varsanyi, D. L. Wood, and A. L. Schawlow, Phys. Rev. Lett. **3**, 544 (1959).

[6] T. H. Maiman, Nature (London) **187**, 493 (1960).

[7] S. Sugano and Y. Tanabe, J. Phys. Soc. Jpn. **13**, 880 (1958).

[8] S. Sugano and I. Tsujikawa, J. Phys. Soc. Jpn. **13**, 899 (1958).

[9] A. A. Manenkov and A. M. Prokhorov, Sov. Phys. JETP **1**, 611 (1955), which gives the spin Hamiltonian of the $^4A_2$ state: $\hat{H} = g_{\|}\mu_B B_z \hat{S}_z + g_{\perp}\mu_B(B_x\hat{S}_x + B_y\hat{S}_y) + D[\hat{S}_z^2 - S(S+1)/3]$; $g_{||} = 1.984 \pm 0.0006$; $g_{\perp} = 1.9867 \pm 0.0006$; $\mu_B =$ Bohr magneton; and $2D = -0.3824$ cm^{-1}.

[10] S. Geschwind, R. J. Collins, and A. L. Schawlow, Phys. Rev. Lett. **3**, 545 (1959).

[11] X. Lu, S. Venugopalan, H. Kim, M. Grimsditch, S. Rodriguez and A. K. Ramdas, Phys. Rev. B **79**, 235204 (2009).

[12] P. A. M. Dirac, *The Principles of Quantum Mechanics*, 4th ed. (Oxford University Press, Oxford, UK, 1958), p. 248.

[13] R. Loudon, *The Quantum Theory of Light*, 3rd ed. (Oxford University Press, Oxford, UK, 2000), Chap. 8.

[14] R. Loudon, Proc. R. Soc. London, Ser. A **275**, 218 (1963).

[15] D. L. Peterson, D. U. Bartholomew, A. K. Ramdas and S. Rodriguez, Phys. Rev. B **31**, 7932 (1985).

[16] See, for example, *Advances in Infrared and Raman Spectroscopy*, Vol. 9, edited by R. J. H. Clark and R. E. Hester (Heyden, London, 1982), Chap. 5, and references therein.

[17] G. M. Williams, P. C. Becker, N. Edelstein, L. A. Boatner, and M. M. Abraham, Phys. Rev. B **40**, 1288 (1989).

[18] S. I. Gubarev, T. Ruf, and M. Cardona, Phys. Rev. B **43**, 1551 (1991).

[19] A. Jayaraman, G. A. Kouroulis, R. People, S. K. Sputz, and L. Pfeiffer, Pramana J. Phys. **35**, 167 (1990).

[20] S.J. Bingham, D. Suter, A. Schweiger, and A. J. Thomson, Chem. Phys. Lett. **266**, 543 (1997).

[21] B. Borger, S. J. Bingham, J. Gutschank, M. O. Schweika, D. Suter, and A. J. Thomson, J. Chem. Phys. **111**, 8565 (1999).

[22] M. O. Schweika-Kresimon, J. Gutschank, and D. Suter, Phys. Rev. A **66**, 043816 (2002).